

Simultaneous organic pollutant degradation and hydrogen peroxide production by molecular-engineered carbon nitride

Chao Xue ^a, Peifang Wang ^a, Huinan Che ^{a,*}, Wei Liu ^a, Bin Liu ^b, Yanhui Ao ^{a,*}

^a Key Laboratory of Integrated Regulation and Resource Development on Shallow Lakes, Ministry of Education, College of Environment, Hohai University, No.1, Xikang road, Nanjing 210098, China

^b Department of Materials Science and Engineering, City University of Hong Kong, Hong Kong SAR 999077, China



ARTICLE INFO

Keywords:

Carbon nitride
Photocatalysis
 H_2O_2 production
Atenolol

ABSTRACT

A novel photocatalytic system was developed for the simultaneous degradation of organic contaminant and generation of H_2O_2 based on molecular-engineered carbon nitride ($AQ-CN_x$). The $AQ-CN_x$ was synthesized by simultaneously introducing N defects and anthraquinone-2-carboxylic acid. Synergistically, the $AQ-CN_x$ exhibited a H_2O_2 production rate of $36.41\text{ mM h}^{-1}\text{ g}^{-1}$, which is 7.87 times as that of CN. More importantly, atenolol (ATL) can promote H_2O_2 production, which in turn increases ATL degradation. Density functional theory (DFT) calculations demonstrate that N defects provide more sites for O_2 adsorption and AQ acts as an electron-acceptor to facilitate the separation of photogenerated electrons and holes. Independent gradient model based on Hirshfeld partition (IGMH) analysis shows that van der Waals interaction between $AQ-CN_x$ and ATL enhances the degradation efficiency. This work provides a new idea for the effective degradation of pollutants and simultaneous generation of H_2O_2 .

1. Introduction

The widespread presence of pharmaceuticals and personal care products (PPCPs) in the natural water environment has attracted strong scientific and public attention in recent years [1,2]. PPCPs, as a new type of contaminant, are water-soluble, difficult to volatilize, and highly resistant to biodegradation [3,4]. Atenolol (ATL), as a beta-blocker PPCP, can be used for the treatment of cardiovascular diseases, but it inhibits the growth of human embryonic cells and is toxic to the membrane system of plants and animals as well as organisms in water, so its ecological impact has received great attention from the research community in recent years [5–8]. Currently, many biological and physico-chemical treatment processes are energy intensive, expensive, and have low removal capacity for ATL. Therefore, it is urgent to develop a green, efficient, and economical technology to degrade ATL.

Advanced oxidation processes (AOPs) hold the promise of efficient treatment of organic pollution compounds [9]. Among them, photocatalytic technology has drawn a lot of interest because of its moderate reaction conditions, high oxidation capacity, and lack of secondary pollutants [10,11]. In the photocatalytic degradation process, the photogenerated electrons and holes migrate to the surface and participate in redox reactions to produce reactive oxygen species (ROS) (e. g. $\bullet O_2$, $\bullet OH$

and H_2O_2) [12,13]. ROS is a strong oxidizing agent and has a good degradation effect on difficult organic pollutants [14,15]. However, it often requires the addition of strong oxidizing agents such as H_2O_2 or O_3 , which increases the economic cost and safety risk [16]. Among many reported photocatalysts, carbon nitride (CN) has the advantages of chemical stability, visible light response and easy preparation, and it can produce ROS ($O_2 \rightarrow \bullet O_2 \rightarrow H_2O_2 \rightarrow \bullet OH$) in situ by activating O_2 molecules [17–20]. Meanwhile many studies use isopropyl alcohol (IPA) and ethanol as hole scavengers to promote the production of H_2O_2 . But the use of IPA not only increases the cost but also has potential environment risk. And the high electrons-holes recombination rate of pure CN also makes the conversion efficiency of $\bullet O_2 \rightarrow H_2O_2 \rightarrow \bullet OH$ low [21].

An increasing number of studies reported methods on CN modification, including morphology modulation, introduction of defects, molecular engineering, and element doping [22–25]. According to previous reports, it has been discovered that introducing defects can capture photogenerated electrons, preventing light-generated electrons and holes from recombining [26]. Additionally, because defects have a large number of localized electrons, they can improve the adsorption and activation of gas molecules [27,28], which further promotes the H_2O_2 production. Nevertheless, although defect is beneficial to improving charge separation, the photocatalytic H_2O_2 production activity is still

* Corresponding authors.

E-mail addresses: chehuinan@hhu.edu.cn (H. Che), andyao@hhu.edu.cn (Y. Ao).

limited. Surprisingly, the CN has π conjugated effect, and the organic monomer with matching structure can be inserted into the 3-s-triazine ring structure by molecular engineering strategy [29]. When the CN is excited by light, the carriers will undergo intramolecular directional movement by the built-in electric field, which effectively enhancing the migration rate of photogenerated carriers [30]. Therefore, the combination of defect and molecular engineering allows efficient electron-hole separation and further promotes the generation of ROS.

In this work, the catalyst AQ-CN_x by introducing N defects and anthraquinone-2-carboxylic acid (AQ-COOH) small molecules was synthesized. N defects tended to increase the light absorption and reduce the band gap, while AQ-COOH was more conducive to achieve efficient electrons-holes separation and O₂ activation. AQ was discovered to encourage the conversion of O₂ to H₂O₂ (AQ + 2H⁺ + 2e⁻ → AQH₂, AQH₂ + O₂ → AQ + H₂O₂), and it acted as an electron-acceptor to facilitate the effective separation of photogenerated electrons and holes. Therefore, the role of introducing N defects and AQ-COOH in CN could improve light absorption capacity, photogenerated carrier separation efficiency and O₂ activation capacity, which improving the performance of photocatalytic H₂O₂ production. Notably, compared with traditional studies on the addition of IPA or ethanol to promote the production of H₂O₂, in the present AQ-CN_x system, not only ATL was used as the hole-trapping agent to promote the H₂O₂ production, but also some H₂O₂ was activated to •OH to further accelerate the degradation of ATL (Scheme 1), shockingly creating a mutually reinforcing synergy. As a result, the development of wastewater treatment was particularly interested in the degradation of contaminants with concurrent H₂O₂ production.

2. Experimental section

2.1. Materials

Melamine (99 %) was purchased from Aladdin. KOH ($\geq 85.0\%$) was purchased from Sinopharm Chemical Reagent Co., Ltd. Acetonitrile (99.0 %) was purchased from Aldrich. Anthraquinone-2-carboxylic acid (98 %) was purchased from Macklin. All reagents used for the synthesis were of laboratory grade and were used without any further purification.

2.2. Synthesis of CN_x photocatalyst

CN_x photocatalysts were synthesized as follows: 15 g of melamine was added into 30 mL of H₂O containing 0.1 g of KOH with stirring for 4 h, and then the resulting solution was dried in an oven at 80 °C overnight. The attained solid mixtures were then put into a crucible covered with a lid after full grinding, and were calcined at 550 °C in a

muffle furnace for 4 h with a heating rate of 10 °C min⁻¹. After cooling down to room temperature, the samples were washed with water to remove any residual alkali. The CN was synthesized by the way that 15 g of melamine was calcined at 550 °C in a muffle furnace for 4 h using a heating rate of 10 °C min⁻¹.

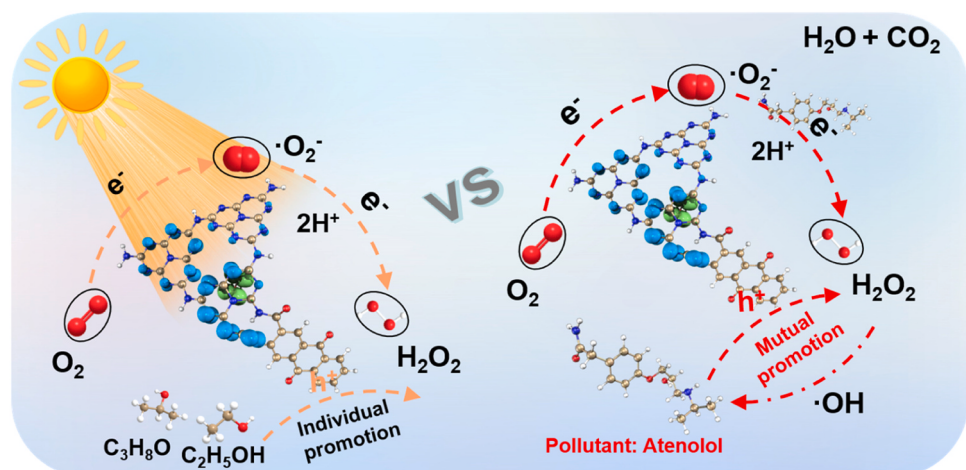
2.3. Synthesis of AQ-CN_x photocatalyst

AQ-CN_x was prepared by adding 0.2 g of as-prepared CN_x photocatalysts and anthraquinone-2-carboxylic acid (60 wt% with respect to CN_x) into 18 mL of acetonitrile. The suspension was ultrasonicated for 30 min, and then was heated and stirred at 50 °C in an oil bath for 12 h. Finally, the suspension was washed several times with DI water and ethanol after cooling down to room temperature, and evaporated to dryness at 60 °C all night to yield the AQ-CN_x sample.

3. Results and discussion

3.1. Structure and morphology analyses

The detailed synthesis diagram of AQ-CN_x was shown in Fig. 1a. Firstly, -C≡N is introduced in CN by thermal polymerization with the addition of KOH, and the -C≡N may be located at one apex of the melon structure of CN. Then the -COOH in AQ reacts with the -NH₂ in CN to form AQ-CN_x. The crystal phases of four samples were characterized by XRD spectra. As shown in Fig. 1b, two diffraction peaks around 12.7° and 27.5° are observed for pure CN, which are assigned to (100) and (002) crystal planes, representing tri-s-triazine ring in-plane compression and interlayer structure stacking, respectively [31]. After the introduction of the N defects, the peak at 12.7° decreases, indicating that N defects result in the loss of ordered structure [32]. When AQ is added, the two peaks are significantly attenuated, indicating that AQ addition reduces the crystallinity of CN within the framework [33]. Then, the molecular structures changes of four samples were detected by FTIR spectroscopy. In Fig. 1c, the peak positions at 810 cm⁻¹, 1250–1750 cm⁻¹ and 3000–3500 cm⁻¹ can be corresponded to the triazine imide units, the stretching vibration modes of aromatic C-N/C≡N heterocycles and overlapping of the stretching vibration of N-H, respectively [34]. Noticeably, a new peak highlighted by the orange shaded regions at 2170 cm⁻¹ occurs in CN_x and AQ-CN_x, which is attributed to an asymmetric stretching vibration of -C≡N [35]. The results indicate N defects were successfully synthesized. Notably, a new peak centered at 702 cm⁻¹ and a small peak at 1680 cm⁻¹ are observed in AQ-CN and AQ-CN_x, corresponding to C-H bending and the C=O bonding by AQ grafting, respectively [36,37]. In addition, ¹³C NMR analysis further provided clear evidence of the introduction of N defects



Scheme 1. The feasible photocatalytic mechanism in the ATL degradation process by AQ-CN_x.

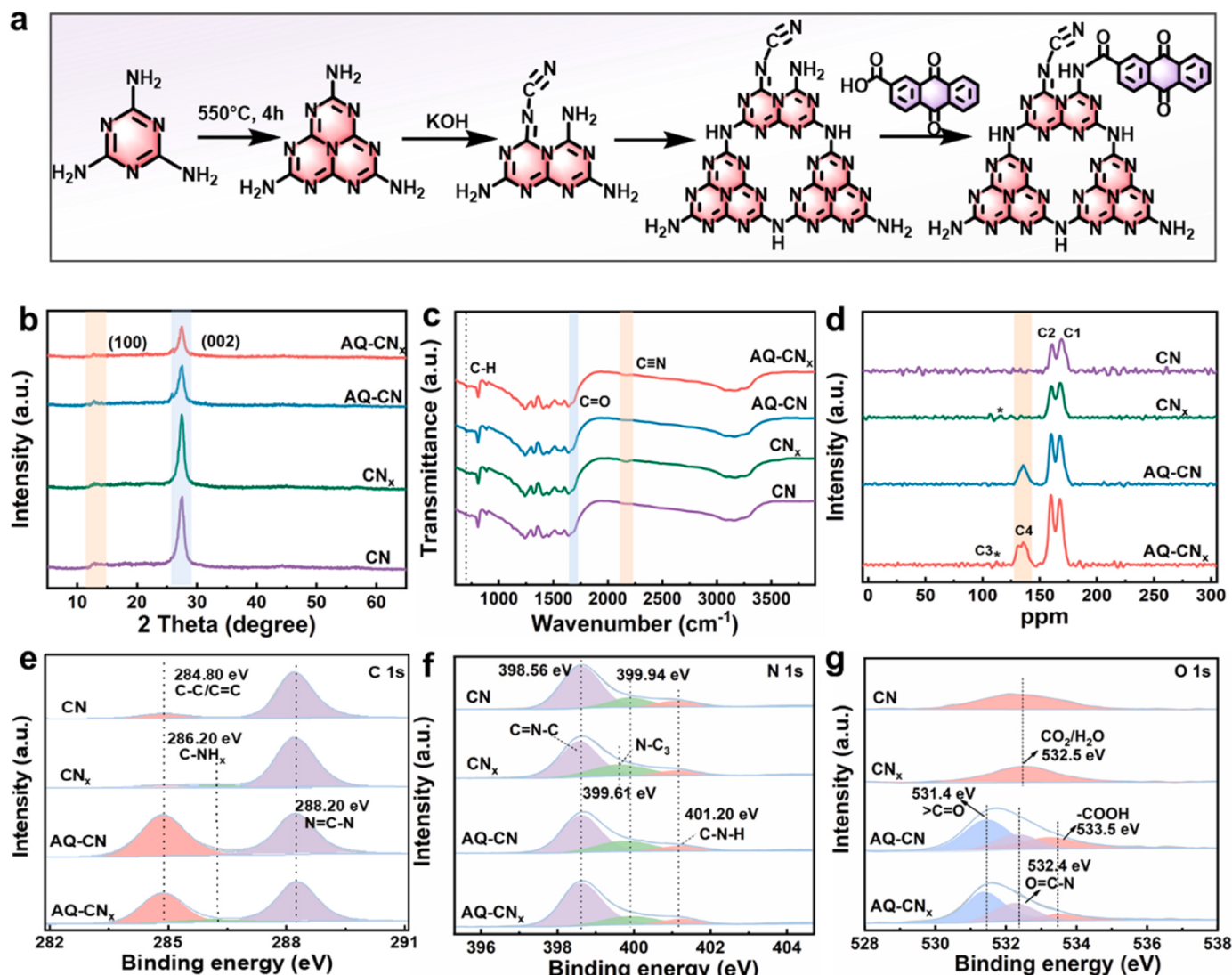


Fig. 1. (a) The detailed synthesis diagrams of AQ-CN_x. (b) XRD pattern (c) FTIR spectroscopy and (d) ¹³C NMR spectra of CN, CN_x, AQ-CN and AQ-CN_x. (e-g) High-resolution XPS spectra of C 1 s, N 1 s, O 1 s, respectively.

and AQ-COOH to CN. Two major peaks located at about 168.0 and 160.1 ppm can be observed for CN (Fig. 1d), which are assigned to the chemical shifts of C_{2N}-NH_x (C2) and C_{3N} (C1) [38]. The peak at approximately 116.3 ppm is found in CN_x and AQ-CN_x, belonging to the C atoms (C3) in -C≡N [39], which demonstrates that N defects were introduced into the structure. In addition, there is a new strong peak (C4) at 134.2 ppm observed for AQ-CN and AQ-CN_x, representing the typical signal of aromatic C=C [40]. This shows that AQ-COOH has been successfully integrated into the CN backbone.

To further investigate the chemical composition of as-prepared catalysts, XPS measurements were also conducted. Compared with CN, the C 1 s spectra of CN_x can be deconvoluted into three components at 284.80 eV, 286.20 eV, and 288.20 eV (Fig. 1e), attaching to the graphitic carbon (C-C/C=C), C-NH_x on the edges of heptazine units and N = C-N, respectively [41]. The new peak at 286.20 eV is ascribed to the introduction of -C≡N, since -C≡N shows similar C1s bind energy to C-NH_x [42]. In addition, there is a stronger aromatic C-C/C=C bonding peak at 284.80 eV observed with AQ-CN and AQ-CN_x due to AQ introduction. For N 1 s XPS spectra (Fig. 1f), three components of CN around 398.56 eV, 399.94 eV, and 401.20 eV are corresponded to C=N-C, N-C₃ and NH_x groups in the heptazine framework, respectively [43,44]. Compared to pure CN, the N-C₃ peak of CN_x has significantly shifted,

indicating a relative content changing of nitrogen atoms in N-C₃ and N=C-N, which could be ascribed as the influence of N defects in the structure [32,42]. In contrast, for O 1 s spectra (Fig. 1g), AQ-CN and AQ-CN_x have two new peaks at 533.5 eV and at 531.4 eV, which are attributed to -COOH and >C=O, respectively [45]. Meanwhile, the amide bond (O=C-N) at 532.4 eV is derived from the reaction between -COOH in AQ and -NH₂ in CN [46]. While the weak peak at 532.5 eV on CN and CN_x is attributed to adsorbed CO₂ or H₂O on the surface [36]. Furthermore, the morphologies of CN, CN_x, AQ-CN and AQ-CN_x were investigated by TEM. As shown in Figs. S1-4, CN shows a block structure, while CN_x, AQ-CN and AQ-CN_x show ultrathin nanosheet structures. Furthermore, the elemental mapping images manifest the uniformity of C, N and O elements distribution in the AQ-CN_x (Fig. S5). Overall, the results of FTIR, ¹³C NMR and XPS consistently illustrate the successful introduction of N defects and the grafting of AQ.

3.2. Photocatalytic H₂O₂ generation

In order to investigate the performance of the as-prepared samples, the photocatalytic H₂O₂ production was measured under visible light ($\lambda > 420$ nm). As shown in Fig. 2a-b, the H₂O₂ yield of pristine CN is only 115.70 μM in an hour. In contrast, the H₂O₂ yield of AQ-CN_x is

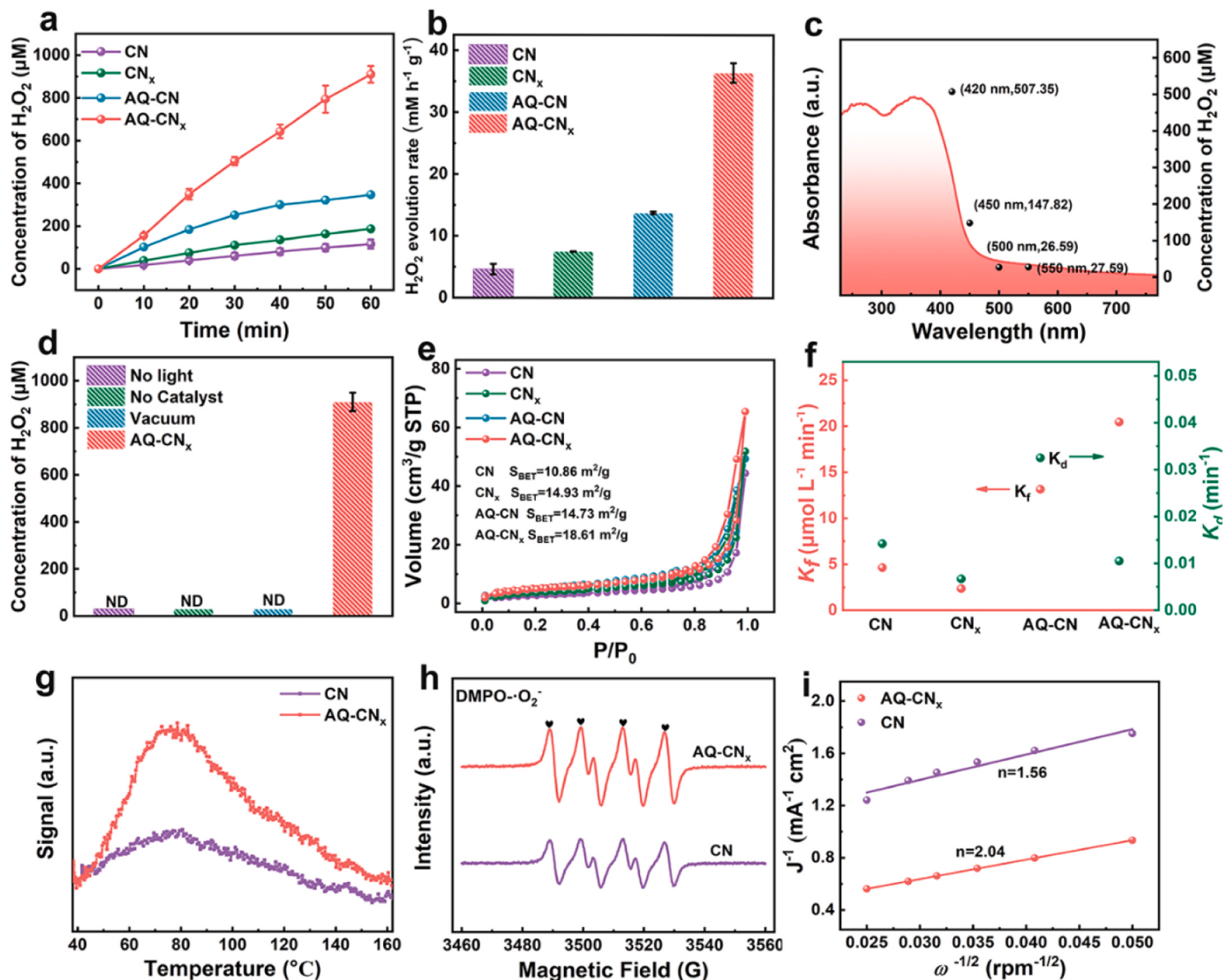


Fig. 2. (a) H₂O₂ production for as prepared samples under visible light irradiation. (b) H₂O₂ production rate of CN, CN_x, AQ-CN and AQ-CN_x. (c) Wavelength dependence of H₂O₂ production with AQ-CN_x. (d) Activity of AQ-CN_x to produce photocatalytic H₂O₂ under various conditions (ND means not detected). (e) N₂ adsorption-desorption isotherms of as prepared samples. (f) Formation rate constant (K_f) and decomposition rate constant (K_d) for H₂O₂ production. (g) O₂-TPD and (h) ESR spectra of DMPO-O₂ for CN and AQ-CN_x. (i) Koutecky-Levich plots of CN and AQ-CN_x.

910.32 μM (corresponding to a rate of 36.41 mM h⁻¹ g⁻¹), which is about 7.87 times as that of CN. The time-dependent absorption spectra of the generated H₂O₂ solution by as-prepared photocatalysts are shown in Fig. S6-9. Subsequently, the H₂O₂ yields at various wavelengths were measured in order to examine the utilization efficiency of sunlight by AQ-CN_x. As shown in Fig. 2c and Fig. S10-11, the concentration of H₂O₂ can reach 27.59 μM at λ = 550 nm, which indicates AQ-CN_x has high utilization rate of sunlight. To further elucidate the real mechanism of H₂O₂ evolution by AQ-CN_x, a series of control experiments were conducted. As demonstrated in Fig. 2d, the H₂O₂ is not detected in the absence of irradiation or photocatalyst, implying that the production of H₂O₂ is a photocatalytic process. In addition, H₂O₂ production is completely suppressed under vacuum. This result shows a decisive role of O₂ in the production of H₂O₂ via oxygen reduction reaction (ORR). Keep in mind that the formation of H₂O₂ by photocatalysis is a dynamic process that involves generation and decomposition. Therefore, the decomposition behavior of H₂O₂ over as-prepared photocatalysts was measured. By using zero-order and first-order kinetics, the formation rate constant (K_f, μmol L⁻¹ min⁻¹) and decomposition rate constant (K_d, min⁻¹) were investigated, which is shown in Eq. (1):

$$[\text{H}_2\text{O}_2] = \frac{K_f}{K_d} (1 - \exp(-K_d t)) \quad (1)$$

In Fig. 2f, the K_f value obviously increases from 4.63 μmol L⁻¹ min⁻¹ (CN) to 20.46 μmol L⁻¹ min⁻¹ (AQ-CN_x). In addition, the K_d value of AQ-CN_x is only 0.0105 min⁻¹, manifesting the increased production of H₂O₂ by AQ-CN_x comes not only from faster formation of H₂O₂ but also from slower decomposition of H₂O₂ (Fig. S12).

To study the reason of the increased H₂O₂ production, the N₂ adsorption-desorption test was done. In contrast to CN, the unique shape of AQ-CN_x results in a greater specific surface area (Fig. 2e), enabling more active sites for the photocatalytic H₂O₂ generation. In addition, AQ-CN_x has stronger O₂-TPD signals (Fig. 2g), indicating that the O₂ adsorption property of AQ-CN_x was markedly enhanced. More importantly, as shown in Fig. 2h, AQ-CN_x exhibits higher DMPO-O₂ signal than CN, demonstrating that AQ-CN_x has improved ability of O₂ production. The effect on the selectivity of the O₂ reduction process was further researched by the rotating disk electrode (RDE) analysis. The linear sweep voltammetry curves (LSV) obtained on RDE of the CN and AQ-CN_x at different rotation speeds are shown in Fig. S13-14.

Subsequently, the electron transfer numbers (n) in ORR pathways were further evaluated by linear regression analyses. The n values of CN and AQ-CN_x are determined to be 1.56 and 2.04 (Fig. 2i), respectively. Especially, the n value for AQ-CN_x is closer to 2, indicating that the AQ-CN_x exhibits a higher selectivity of two-step single-electron O₂ reduction for the H₂O₂ generation. In addition, compared the photocatalytic performance of AQ-CN_x with other CN based materials for H₂O₂ production (Table S1), the AQ-CN_x has surpassed most of the photocatalysts reported to date in H₂O₂ production. The above results suggest that the introduction of N defects and AQ can optimize the activity on photocatalytic H₂O₂ production.

What's more, it is essential to conduct photocatalytic reactions at the same average photon absorption rate since the photon absorption rate of the catalyst is one of the crucial elements impacting the photocatalytic activity [47,48]. The average extinction coefficients are calculated according to the Lambert-Beer law [49]:

$$A = \varepsilon bc \quad (2)$$

Where A is absorbance, ε refers to extinction coefficient, b is optical path length and c means concentration of light absorbing substance. The absorbances of as-prepared catalysts in aqueous suspension are shown in Fig. S15a. The average extinction coefficients of CN, CN_x, AQ-CN, and AQ-CN_x are calculated to be 2780, 5000, 3460 and 3790 cm²/g. The optimum range of τ in the photocatalytic system was 1.8–4.4 [50]. In all experiments, the reactor is a cylinder with an inner wall diameter of 5.1 cm. According to the formula $\tau = hce$ (h , c , and e refer to depth of liquid in the system, catalyst concentration, and average extinction coefficient) [51], the τ of CN, CN_x, AQ-CN, and AQ-CN_x are calculated to be 3.3, 6.0, 4.1 and 4.5, respectively. To make a meaningful comparison

between the catalysts at equal "optical thickness", We set optical thickness to 4, according to the formula $\tau = hce$, the concentrations of CN, CN_x, AQ-CN, and AQ-CN_x are set to 0.60, 0.33, 0.48 and 0.44 g/L. At the same optical thickness, AQ-CN_x shows excellent photocatalytic performance. The AQ-CN_x outperforms all other as-prepared catalysts in terms of generating H₂O₂ (Fig. S15b).

3.3. Photocatalytic ATL degradation simultaneous H₂O₂ generation

Although IPA can promote the production of H₂O₂, extensive use of it results in environmental pollution. Therefore, the use of pollutants as sacrificial agents was investigated to achieve the degradation of pollutants while promoting the H₂O₂ production. In order to investigate whether ATL can be used as a sacrificial agent to promote the production of H₂O₂, the effect of different concentrations of ATL on the production of H₂O₂ over AQ-CN_x was investigated. As shown in Fig. 3a, the production of H₂O₂ increases with the increase of ATL concentration. Under pure water, the H₂O₂ production of AQ-CN_x is 60.08 μM in 1 h, and surprisingly, the H₂O₂ production could reach 136.45 μM in 50 ppm ATL, which is 2.27 times as that under pure water. This result indicates that ATL can be used as a sacrificial agent to promote the production of H₂O₂. In addition, the degradation effect of AQ-CN_x on ATL was also investigated. As shown in Fig. 3b, it can be found that the ATL with concentrations of 10 and 20 ppm are substantially degraded in 10 min, and the degradation rate of 50 ppm of ATL reaches 87 % in 1 h. Therefore, it is hypothesized that there is a synergistic effect that photogenerated e⁻ and h⁺ are generated in the AQ-CN_x system under light. Then, part of the h⁺ oxidizes ATL, promoting the effective separation of electrons and holes, and further enhancing the production of H₂O₂.

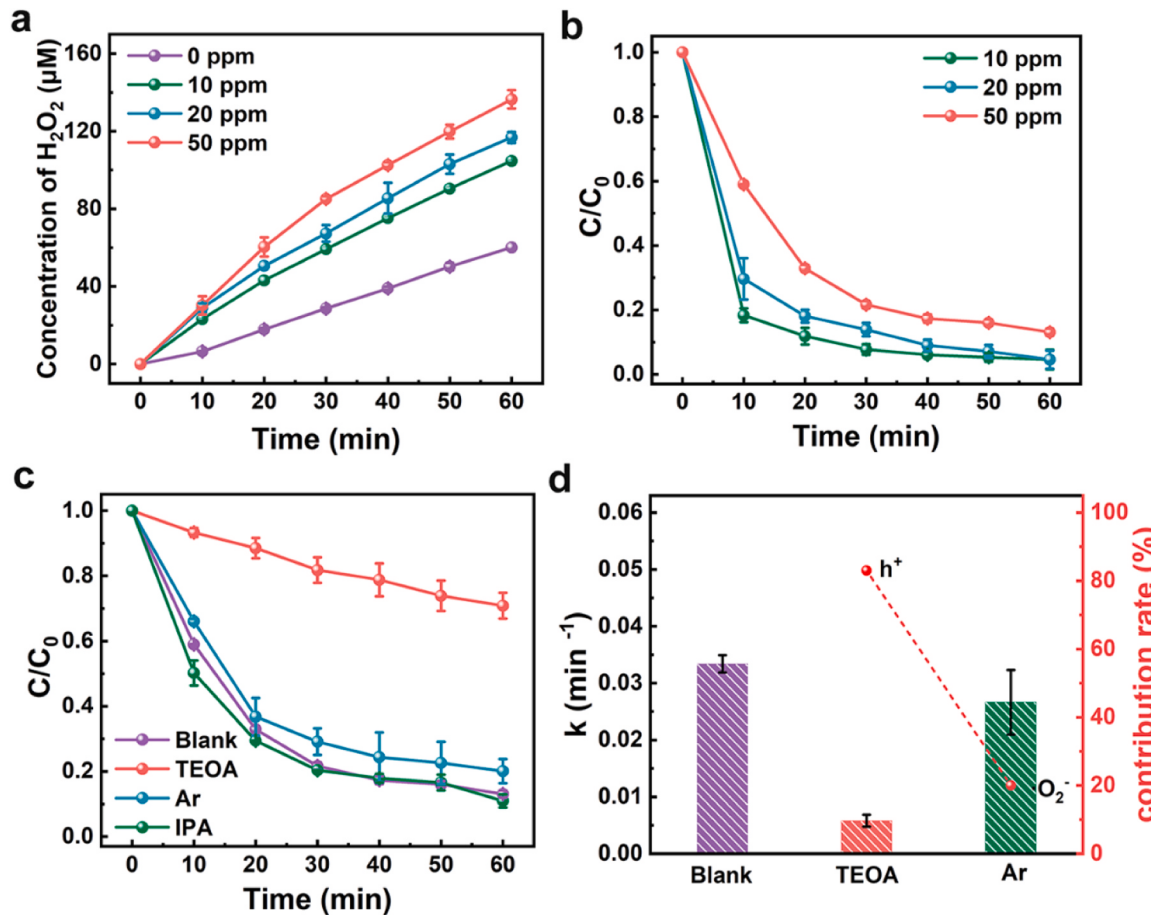


Fig. 3. (a) Yield of H₂O₂ at different concentrations of ATL over AQ-CN_x. (b) Degradation of ATL over AQ-CN_x. (c) Effects of a series of scavengers on the degradation of ATL. (d) Degradation kinetics and the contributions of h⁺ and O₂⁻ for degradation of ATL over AQ-CN_x.

To prove this speculation, capture experiments were performed. As present in Fig. 3c, triethanolamine (TEOA), argon (Ar) and isopropanol (IPA) are used to probe the effect of h^+ , $\cdot\text{O}_2$ and $\cdot\text{OH}$, respectively. It can be found that the degradation rate of ATL is drastically reduced with the addition of TEOA. When Ar is passed, the degradation of ATL is inhibited by a small amount. While the degradation percent increases a little when IPA is added, which may be attributed to the fact that IPA promotes the production of H_2O_2 , then H_2O_2 is decomposed into $\cdot\text{OH}$, thus increasing the degradation rate. This phenomenon indicates that the active substances that play major roles in the degradation of ATL are the h^+ and $\cdot\text{OH}$. In addition, the contribution rate of each active substance to ATL degradation was obtained by calculating the degradation rate constant of ATL under different trapping agents. The formula is as follows [52]:

$$\ln(C_0/C_t) = K_{app}t \quad (3)$$

$$Rh^+ = \frac{K_{h^+}}{K_{app}} = \frac{K_{app} - K_{TEOA}}{K_{app}} \quad (4)$$

$$R\cdot O_2^- = \frac{K_{\cdot O_2^-}}{K_{app}} = \frac{K_{app} - K_{Ar}}{K_{app}} \quad (5)$$

According to the calculated results, the contribution of h^+ to the degradation of ATL is found to be 83 %, while the $\cdot\text{O}_2$ is 20 % (Fig. 3d). In Fig. S16–17, the lower signal intensity in TEMPO- h^+ represents more h^+ content under light, and the higher DMPO- $\cdot\text{OH}$ signal under light indicates more $\cdot\text{OH}$ can be generated in AQ-CN_x, which further proves the

above conclusion. Finally, the results illustrate that AQ-CN_x exhibited good stability (Fig. S18–20). The above results prove that ATL can be used as sacrificial agents to promote the production of H_2O_2 .

3.4. The degradation mechanism of ATL

The interaction between AQ-CN_x and ATL is graphically revealed by independent gradient model based on Hirshfeld partition (IGMH) analyses [53]. IGMH clearly shows the interaction between AQ-CN_x and ATL. As shown in Fig. 4a-b, there is a large green equivalence surface between the two layers, which undoubtedly indicates that the combination of AQ-CN_x and ATL layers relies on a broad π - π stacking interaction. The plot between δg^{inter} and $\text{Sign}(\lambda_2)\rho$ for the structures is shown in Fig. 4c, in which blue, green and red represent strong attraction, van der Waals force and strong repulsion, respectively. It also indicates that there is a van der Waals interaction between AQ-CN_x and ATL. During photodegradation, this weak interaction helps to facilitate the transfer of electrons to the O_2 and holes to the ATL, resulting in a significantly enhanced photodegradation efficiency of ATL [54]. These results indicate that AQ-CN_x has excellent degradation activity for ATL.

In order to better understand the degradation mechanism of ATL, the reactive sites of the ATL molecule were anticipated by DFT calculation. The molecular structure of ATL is exhibited in Fig. 5a, including benzene ring, amine groups and amides. Then, as shown in Fig. 5b and c, the HOMO orbital of ATL is primarily found in the benzene ring, carbonyl group, O1 and N4 region, whilst its LUMO orbital tends to cluster in the benzene ring. The ESP reflecting the surface electron cloud distribution

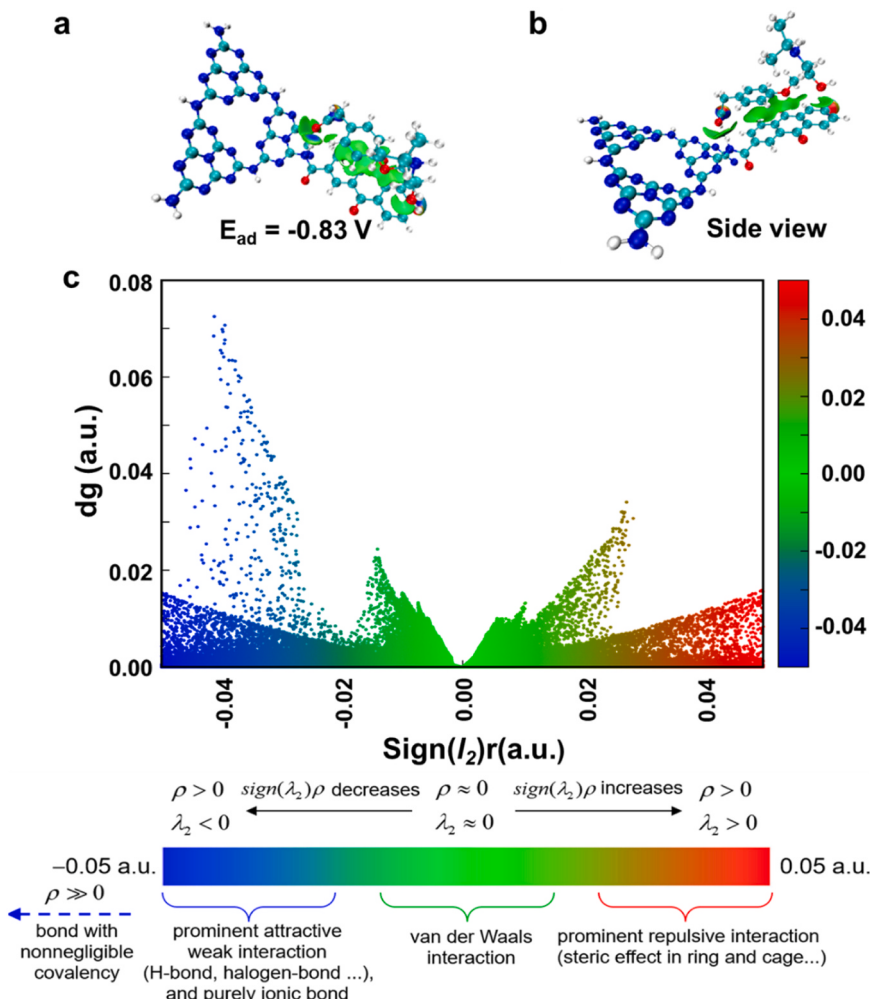


Fig. 4. (a-b) $\text{Sign}(\lambda_2)\rho$ colored isosurface of $\delta g^{\text{inter}} = 0.005$ a.u. of ATL adsorbed AQ-CN_x corresponding to IGMH analyses. (c) Scatter map between $\text{Sign}(\lambda_2)\rho$ and δg .

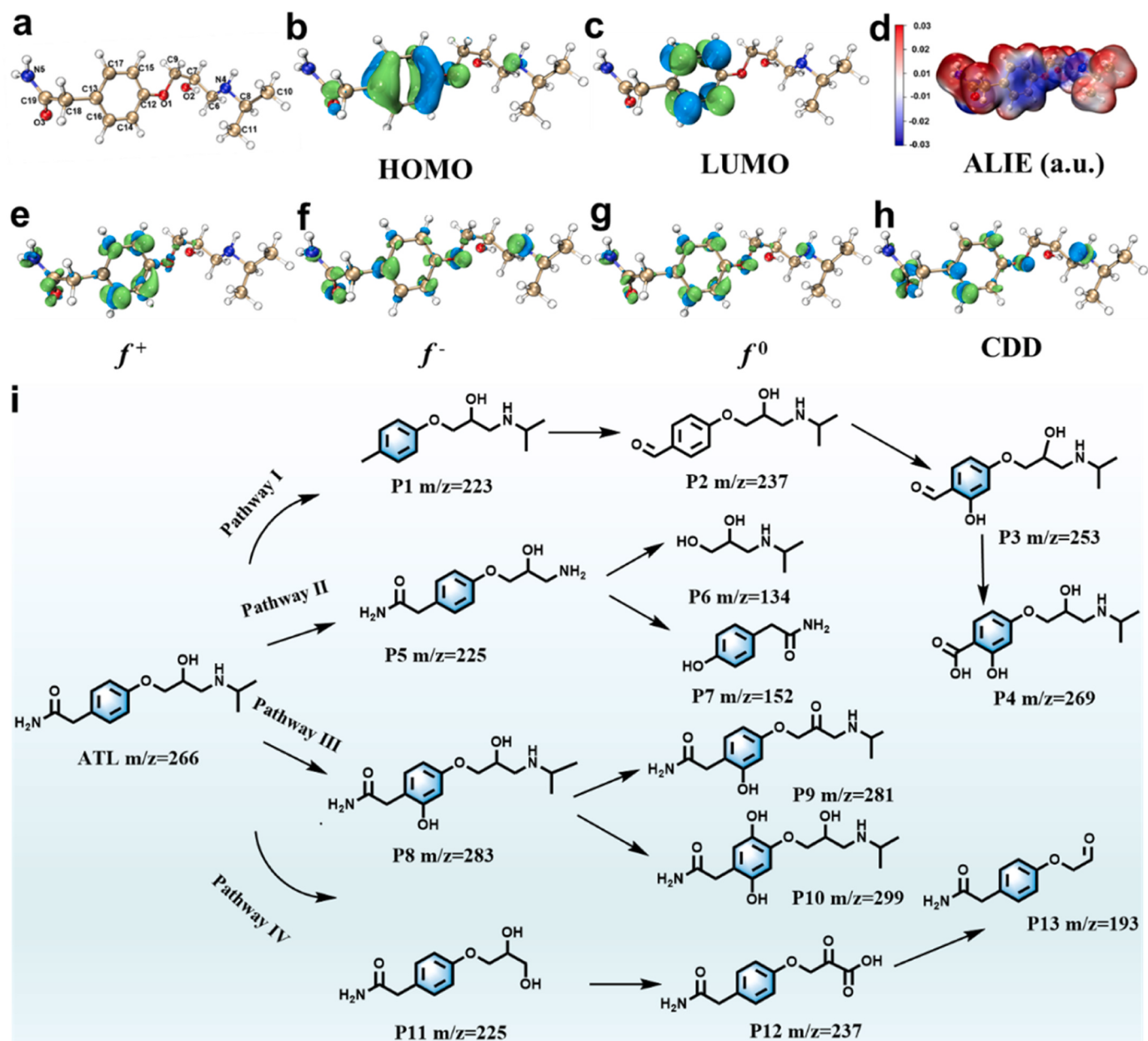


Fig. 5. (a) Optimized structure of ATL, (b) HOMO, (c) LUMO and (d) ESP of ATL. The isosurface of (e) f^+ , (f) f^- , (g) f^0 and (h) CDD of ATL. (i) Possible degradation pathways of ATL.

of ATL is showed in Fig. 5d. It's worth noticing that the blue area is an electron-rich region that electrophilic reagents (h^+ , $\cdot\text{OH}$) might easily attack, and the red area is an electron-poor region that is vulnerable to assault by nucleophilic chemicals ($\cdot\text{O}_2$). In addition, Hirshfeld charge and Fukui index (f^+ , f^- and f^0) are used to analyze the regioselectivity of active species to ATL molecule. As depicted in Fig. 5e-g, atoms with higher values of f^+ , f^- and f^0 are more vulnerable to be attacked by nucleophilic species ($\cdot\text{O}_2$), electrophilic species (h^+ and $\cdot\text{OH}$) and free radicals ($\cdot\text{O}_2$ and $\cdot\text{OH}$), respectively [55,56]. Moreover, the CDD also shows the distribution of nucleophilic and electrophilic sites (Fig. 5h). Obviously, the C15 and C16 have nucleophilicity, while C13, O1 and N4 have electrophilicity. And the f^+ , f^- and f^0 based on Hirshfeld charges distribution of ATL are illustrated in Table S2.

To explore the main intermediate products in the photodegradation of ATL, the liquid chromatography-mass spectrometry (LC-MS) was carried out (Fig. S21). Based on the DFT calculation, four possible degradation pathways of ATL were proposed, as shown in Fig. 5i. In

pathway I, the amide group was attacked by $\cdot\text{OH}$ to produce P1 ($m/z = 223$), and the carbon radical was further oxidized to form P2 ($m/z = 237$) [57]. Subsequently, P3 ($m/z = 253$) was formed through further hydroxylation. And P3 was attacked by $\cdot\text{OH}$, resulting in the production of P4 ($m/z = 269$). Besides, in pathway II, the $\cdot\text{OH}$ could attack the secondary amine structure of ATL, which would rupture the C-N bond and result in the formation of P5 ($m/z = 225$). And the attack of $\cdot\text{OH}$ would cause the ether bond to cleave, producing P6 ($m/z = 134$) and P7 ($m/z = 152$) [6]. In pathway III, $\cdot\text{OH}$ may attack the aromatic ring of ATL, leading to arising the hydroxylated product P8 ($m/z = 283$). Then the hydroxyl group of P8 might be oxidized to a ketone group by dissolved O_2 , yielding P9 ($m/z = 281$). And part of P8 was further hydroxylated to form P10 ($m/z = 299$) [58]. In pathway IV, when h^+ attacked the ATL molecule, yielding P11 ($m/z = 225$). Intermediate P11 was further oxidized to generate P12 ($m/z = 237$), which was then decarboxylated to form P13 ($m/z = 193$). The system's active radicals further degraded the intermediates, which eventually mineralized into

CO_2 and H_2O .

To further investigate the degradation of ATL by AQ-CN_x , three-dimensional excitation-emission matrix fluorescence spectra (3D EEMs) experiment was carried out. As shown in Fig. S22, the emission (E_m) peak of ATL is located at 300–350 nm and the excitation (E_x) peak is located around 200–300 nm. The peak intensity gradually decreases, indicating that the ATL is degraded. Notably, there is a new excitation peak appearing at 400–450 nm, and this peak intensity increases as the degradation time increases, meaning intermediates are being formed.

3.5. Mechanism of enhanced photocatalytic activity

To reveal the mechanism for the excellent catalytic performance of AQ-CN_x , photoelectrochemistry was conducted to probe the carrier separation efficiency and band structure. The recombination of photo-induced charge carriers which is essential to the catalytic performance of samples was measured by PL. As plotted in Fig. 6a, upon photoexcitation at 350 nm, the CN_x exhibits a lower PL intensity than CN, indicating that the recombination of photogenerated electron-hole pairs is effectively inhibited after N defects introduction [59]. What's more, the fact that AQ-CN_x has a weakest PL intensity is ascribed to the stronger

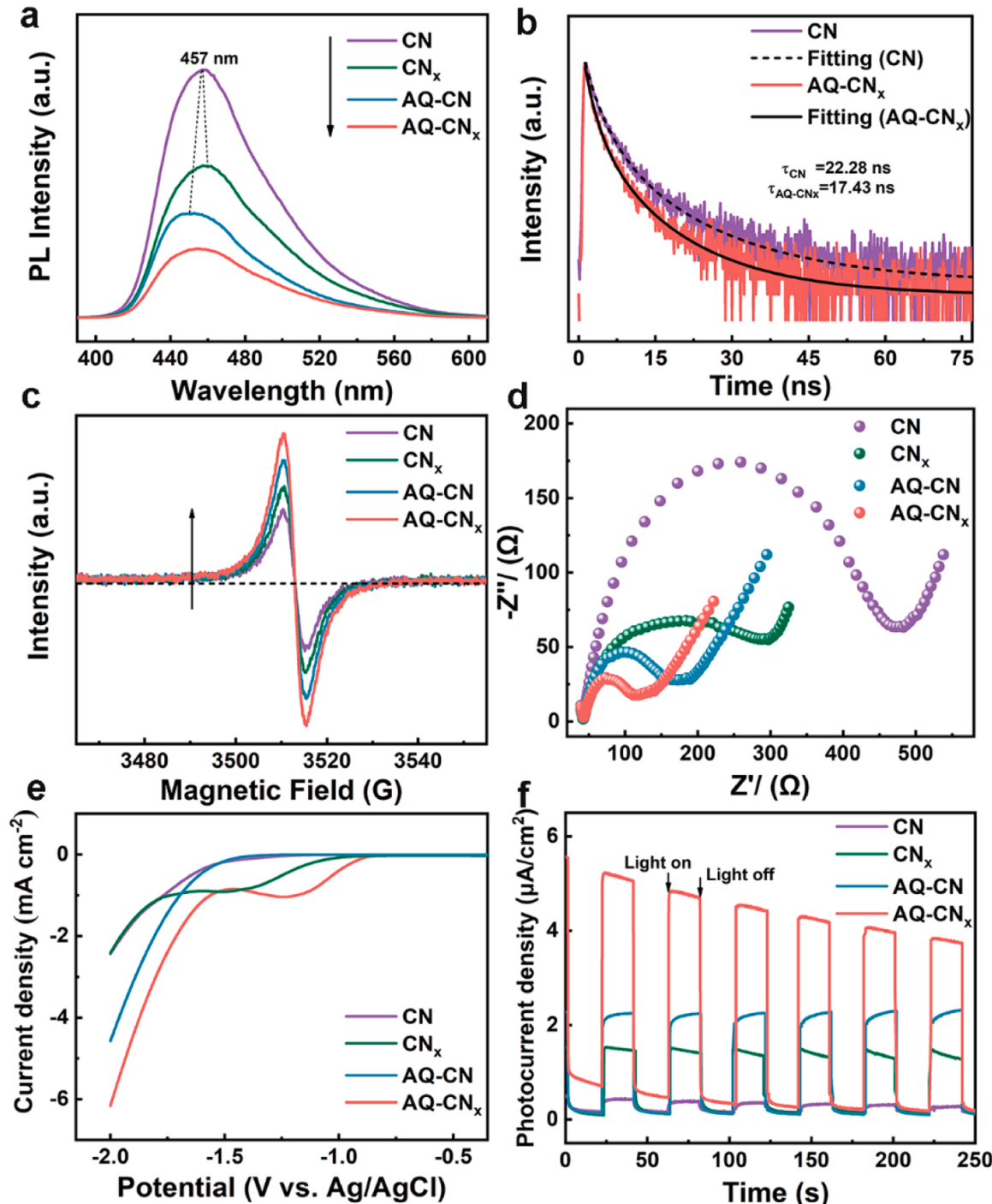


Fig. 6. (a) PL spectra of four samples. (b) Time-resolved fluorescence spectra of CN and AQ-CN_x . (c) EPR signal intensity for as prepared samples. (d) EIS plots, (e) LSV curves and (f) TPC curves of four samples.

electron-withdrawing ability of AQ-COOH, which is beneficial for separation and transfer efficiency of the photogenerated carriers, ultimately enhancing photocatalytic efficiency. This improvement is further corroborated by the comparative time-resolved PL spectroscopy analysis. As shown in Fig. 6b and Fig. S23, the calculated lifetime of CN and CN_x is 22.28 ns and 21.99 ns, while the lifetimes of AQ-CN and AQ- CN_x is 20.89 ns and 17.43 ns. This finding implies that N defects and AQ can shorten the average lifespan of charge. This result also implies that an additional nonradiative decay channel may be opened through the electron transfer from CN to AQ and reinforce the charge separation and migration [60]. UV-vis diffuse reflection spectra (DRS) were applied to analyze light absorption property of samples. As shown in Fig. S24a, relative to CN, the intrinsic absorption edge of CN_x shows a red shift, which indicating N defects can increase the visible light absorption efficiency. In addition, the corresponding Kubelka-Munk plots are shown in Fig. S24b, the band gaps can be derived as 2.61 eV, 2.56 eV, 2.63 eV and 2.59 eV for CN, CN_x , AQ-CN and AQ- CN_x , respectively. Whereafter, Mott-Schottky curves were employed in order to estimate the semiconductor's flat band potentials (E_{FB}) [61]. As seen in Fig. S25, the E_{FB} values are determined at -1.27 V and -1.23 V for CN and AQ- CN_x (vs. Ag/AgCl). As report goes, the conduction band potential (E_{CB}) for n-type semiconductors is thought to be 0.1 V higher than E_{FB} [62]. So, the E_{CB} of CN and AQ- CN_x are -1.17 V and -1.13 V , respectively. The E_{CB} values are greater than the potential for O_2 reduction. Combining the calculated bandgap and E_{CB} values of catalysts, the valance band (VB) position can be deduced. Band distribution of each sample is shown in Fig. S26. It's worth noting that N defects could narrow the band gap of CN, as a result, valence band electron excitation in CN_x will be significantly simpler than in CN. Surprisingly, the introduction of AQ does not reduce the band gap, but makes the E_{CB} value larger, which is more conducive to O_2 reduction.

In addition, the orphaned electron on the carbon atoms of the aromatic rings carbon nitride can be discovered utilizing EPR spectroscopy [63]. As shown in Fig. 6c, AQ- CN_x possesses a much stronger signal than CN, revealing that there are more unpaired electrons in AQ- CN_x , which is caused by the N atom loss and the strong electron-withdrawing characteristics of AQ. According to reports, the concentration of delocalized electrons aids in the promotion of the production of photogenerated active radical species, hence enhancing photocatalytic activity [64]. In the case of assessing charge transfer, EIS was further measured. It is well known that a smaller arc radius normally represents a smaller transfer resistance of photogenerated charge [65]. In Fig. 6d, N defects can further weaken the charge transfer resistance of CN, and the AQ- CN_x owns smaller arc radius than others, indicating that AQ coupling is also beneficial to accelerating the transfer efficiency of the internal charge. The LSV curve is shown in Fig. 6e, and the AQ- CN_x has highest current density, indicating AQ- CN_x is equipped with higher charge separation efficiency. In addition, the photocurrent was measured to further evaluate the carrier separation efficiency. As shown in Fig. 6f, the photocurrent response of the samples shows a good reproducibility for repeated on/off cycles, and AQ- CN_x has the highest photocurrent density, indicating higher carrier separation efficiency [66], which is attributed to that AQ as an electron acceptor promotes the separation of electrons and holes. From the photoelectrochemical performance results, the introduction of N defects and AQ can accelerate the separation of e^- and h^+ , thus promoting the photocatalytic activity of the catalysts.

The feasible photocatalytic mechanism that AQ- CN_x increases ATL degradation while simultaneously producing H_2O_2 is proposed in Fig. S27. Firstly, the photogenerated electrons are excited from VB to CB under light irradiation, and the holes stay on the VB position of AQ- CN_x . While a portion of photo-generated electrons and holes recombine in the body, and the remainder are swiftly and spatially separated and transported to the surface of AQ- CN_x . Then the electrons on CB can reduce the O_2 to $\cdot\text{O}_2$ ($\text{O}_2/\cdot\text{O}_2 = -0.33\text{ V}$), and $\cdot\text{O}_2$ is reduce to H_2O_2 ($\cdot\text{O}_2/\text{H}_2\text{O}_2 = 0.68\text{ V}$). And the holes in the VB of AQ- CN_x could directly degrade ATL,

which hastens the separation of electrons and holes, further improving H_2O_2 production. What's more, H_2O_2 can be decomposed into $\cdot\text{OH}$ to degrade ATL, therefore oxidizing and degrading ATL to smaller molecule products.

3.6. DFT calculations

The introduction of N defects and AQ can accelerate the separation of e^- and h^+ , which allows electrons to reduce O_2 to produce H_2O_2 and holes to oxidize ATL, enhancing H_2O_2 production and ATL degradation. To gain a thorough understanding of the mechanism underlying H_2O_2 production by $2e^-$ ORR, DFT simulations were done. Firstly, AQ- CN_x shows that HOMO and LUMO are distributed on different structures compared to CN, indicating that there is a spatial separation of HOMO and LUMO (Fig. 7a and Fig. S28). Secondly, it is found that the electrons-holes distribution of CN is uniform, indicating that the fast electrons-holes complexation is the main reason for the low activity. While, electrons-holes distribution is on different structures over AQ- CN_x . The holes of AQ- CN_x are distributed on CN and the electrons are distributed on AQ, indicating AQ as an electron acceptor (Fig. S29-30) is favorable to improve the efficiency of electrons and holes separation, which is a testament to AQ's strong ability to absorb electrons. To further reveal the changes in the energy band structure, the density of states (DOS) was investigated. It is found that the energy band gap of AQ- CN_x is reduced compared to CN and is more negative in energy upon adsorption of O_2 (Fig. S31-32 and Fig. 7b-c), suggesting that electrons are more easily transferred to the π^* orbitals of O_2 [67]. In order to further reveal the activation mechanism of O_2 in the process of electron excitation, its excited state is explored and it is found that electrons are concentrated on O_2 to promote O_2 activation (Fig. 7d-e). Obviously, the number of electron (n) migrated from AQ- CN_x to O_2 in every excitation state is higher than that of CN, thus accelerating activation of O_2 . The electronic structure of O_2 adsorption reveals β orbitals are distributed on O_2 , indicating the electrons of β spin orbitals are more easily transferred directly to π^* orbitals of O_2 (Fig. S33-34) [68]. From all the results, AQ- CN_x can give a boost to the activation of O_2 , triggering ultrahigh photocatalytic H_2O_2 generation efficiency for AQ- CN_x .

4. Conclusion

In summary, AQ- CN_x was constructed by introducing small molecule AQ-COOH and N defects to promote the H_2O_2 production performance of CN. PL, electrochemical and DFT calculations results have proven that the electrons-holes separation efficiency is successfully enhanced, indicating AQ as an electron acceptor promotes the separation of electrons and holes by withdrawing electrons. While O_2 -TPD has proven the O_2 adsorption is strengthened by introducing small molecule AQ-COOH and N defects. Therefore, AQ- CN_x has improved photogenerated carrier separation efficiency and O_2 adsorption capacity, which improves the performance of photocatalytic H_2O_2 production. The rate of H_2O_2 production can reach $36.41\text{ mM h}^{-1}\text{ g}^{-1}$, which is about 7.87 times as that of CN. In addition, in the AQ- CN_x system, the ATL is used as the hole trapping agent to promote the production of H_2O_2 , while the degradation percent of 50 ppm ATL can reach 87 % in 1 h. What's more, DFT calculations confirm the electrons of β spin orbitals are more easily transferred directly to π^* orbitals of O_2 over AQ- CN_x to improve O_2 activation. The synergistic mechanism is of great significance for the removal of pollutants from wastewater and the simultaneous generation of H_2O_2 .

CRediT authorship contribution statement

Chao Xue: Methodology, Software, Validation, Visualization, Writing - Original Draft. **Peifang Wang:** Validation, Formal analysis, Writing - Review & Editing. **Huinan Che:** Validation, Visualization, Formal analysis, Writing - Review & Editing. **Wei Liu:** Formal analysis,

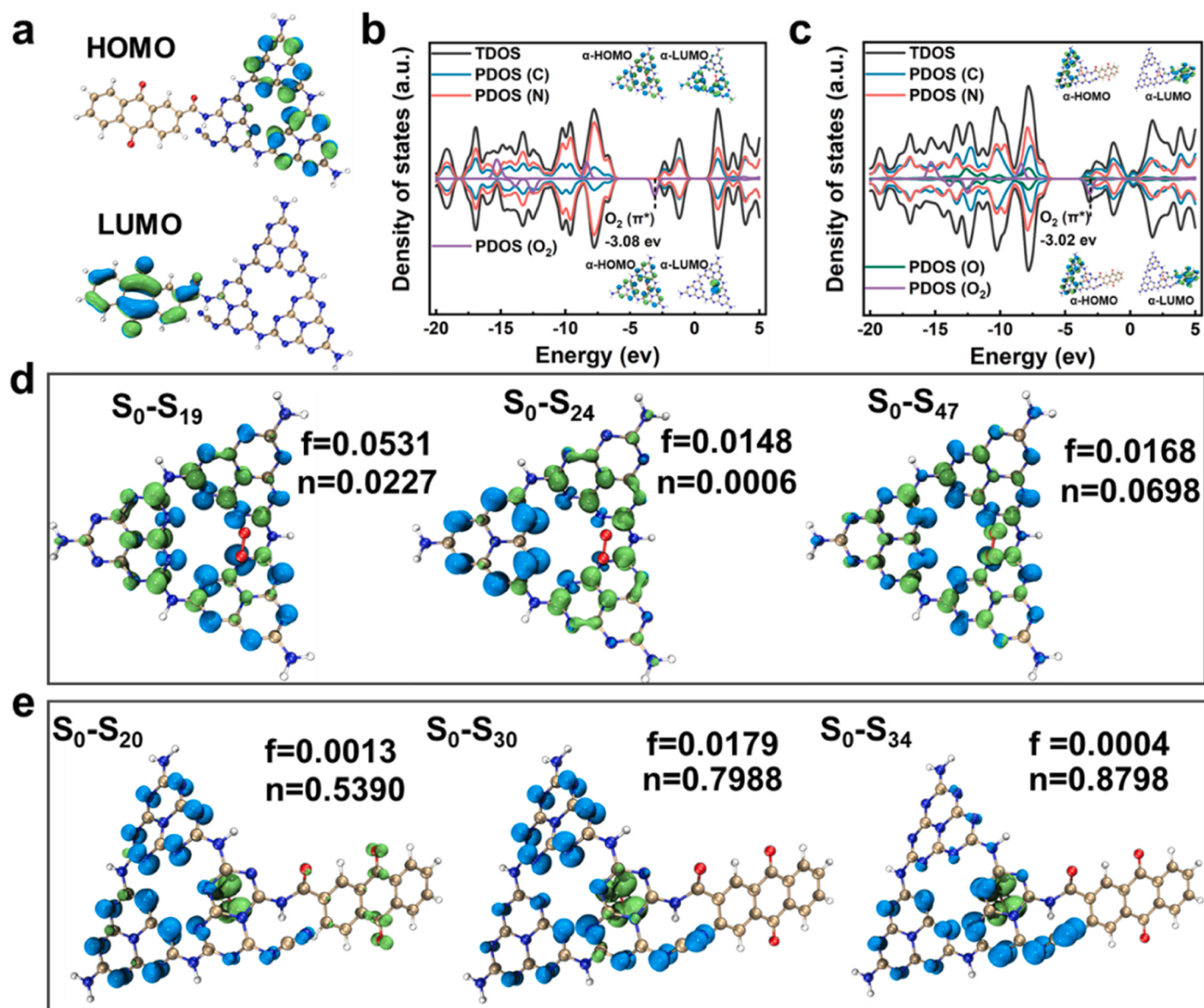


Fig. 7. (a) Electronic structure of the optimized HOMO and LUMO of AQ-CN_x. Gray, blue, white and red represent C, N, H and O, respectively. (b), (c) Total DOS and PDOS of O₂ adsorbed CN and AQ-CN_x; The α/β HOMO and α/β LUMO of O₂ adsorbed CN and AQ-CN_x are shown in the inset; The isosurface value is 0.03 e/ \AA^3 . (d-e) Electron-hole distribution of O₂ adsorbed CN and AQ-CN_x in different excited states (green isosurface: electron distribution and blue isosurface: hole distribution), the isosurface value is 0.002 e/ \AA^3 .

Writing - Review & Editing. **Bin Liu:** Writing - Review & Editing, Formal analysis. **Yanhui Ao:** Conceptualization, Writing - Review & Editing, Supervision, Funding acquisition, Formal analysis.

Declaration of Competing Interest

The authors declare that they have no known competing financial interests or personal relationships that could have appeared to influence the work reported in this paper.

Data availability

Data will be made available on request.

Acknowledgements

We are grateful for grants from Natural Science Foundation of China (51979081, 52100179), Fundamental Research Funds for the Central

Universities (B210202052), National Science Funds for Creative Research Groups of China (No. 51421006), and PAPD.

Appendix A. Supporting information

Supplementary data associated with this article can be found in the online version at doi:10.1016/j.apcatb.2023.123259.

References

- [1] W.K. Zhang, T. Huang, Y. Ren, S. Yang, X.Y. Zhao, M.S. Yuan, J.Y. Wang, Q. Tu, A multifunctional chitosan composite aerogel for PPCPs adsorption, Carbohydr. Polym. 298 (2022), 120102.
- [2] X. Shi, B. Ren, X. Jin, X.C. Wang, P.K. Jin, Metabolic hazards of pharmaceuticals and personal care products (PPCPs) in sewers, J. Hazard. Mater. 432 (2022), 128539.
- [3] J.L. Liu, M.H. Wong, Pharmaceuticals and personal care products (PPCPs): a review on environmental contamination in China, Environ. Int. 59 (2013) 208–224.
- [4] X.W. Liu, T.Q. Zhang, L.L. Wang, Y. Shao, L. Fang, Hydrated electron-based degradation of atenolol in aqueous solution, Chem. Eng. J. 260 (2015) 740–748.

- [5] J.C.G. Sousa, A.R. Ribeiro, M.O. Barbosa, M.F.R. Pereira, A.M.T. Silva, A review on environmental monitoring of water organic pollutants identified by EU guidelines, *J. Hazard. Mater.* 344 (2018) 146–162.
- [6] X.P. Yu, W.L. Qin, X.J. Yuan, L. Sun, F. Pan, D.S. Xia, Synergistic mechanism and degradation kinetics for atenolol elimination via integrated UV/ozone/peroxymonosulfate process, *J. Hazard. Mater.* 407 (2021), 124393.
- [7] A.A. Godoy, F. Kummrow, P.A.Z. Pamplin, Occurrence, ecotoxicological effects and risk assessment of antihypertensive pharmaceutical residues in the aquatic environment—a review, *Chemosphere* 138 (2015) 281–291.
- [8] Y.Q. Gao, N.Y. Gao, J.X. Chen, J. Zhang, D.Q. Yin, Oxidation of β -blocker atenolol by a combination of UV light and chlorine: kinetics, degradation pathways and toxicity assessment, *Sep. Purif. Technol.* 231 (2020), 115927.
- [9] T. Li, L. Zhou, Improving heterogeneous Fenton reactivity of schwertmannite by increasing organic carbon and its promising application, *Environ. Funct. Mater.* 1 (2022) 160–165.
- [10] Q. Zhang, J. Chen, X. Gao, H.N. Che, P.F. Wang, Y.H. Ao, In-depth insight into the mechanism on photocatalytic synergistic removal of antibiotics and Cr (VI): the decisive effect of antibiotic molecular structure, *Appl. Catal. B: Environ.* 313 (2022), 121443.
- [11] G.S. Liu, Y.N. Zhou, J. Teng, J.N. Zhang, S.J. You, Visible-light-driven photocatalytic activation of peroxymonosulfate by $\text{Cu}_2(\text{OH})\text{PO}_4$ for effective decontamination, *Chemosphere* 201 (2018) 197–205.
- [12] R. Chen, J. Chen, H.N. Che, G. Zhou, Y.H. Ao, B. Liu, Atomically dispersed main group magnesium on cadmium sulfide as the active site for promoting photocatalytic hydrogen evolution catalysis, *Chin. J. Struct. Chem.* 41 (2022) 2201014–2201018.
- [13] Y.L. Liao, J. Bräme, W.X. Que, Z.M. Xiu, H.X. Xie, Q.L. Li, M. Fabian, P.J. Alvarez, Photocatalytic generation of multiple ROS types using low-temperature crystallized anodic TiO_2 nanotube arrays, *J. Hazard. Mater.* 260 (2013) 434–441.
- [14] H.K. Yang, W.Y. Wang, X. Wu, M.S. Siddique, Z.Y. Su, M.J. Liu, W.Z. Yu, Reducing ROS generation and accelerating the photocatalytic degradation rate of PPCPs at neutral pH by doping Fe-N-C to g-C₃N₄, *Appl. Catal. B: Environ.* 301 (2022), 120790.
- [15] Y.W. Guo, C.P. Cheng, J. Wang, Z.Q. Wang, X.D. Jin, K. Li, P.L. Kang, J.Q. Gao, Detection of reactive oxygen species (ROS) generated by $\text{TiO}_2(\text{R})$, $\text{TiO}_2(\text{R/A})$ and $\text{TiO}_2(\text{A})$ under ultrasonic and solar light irradiation and application in degradation of organic dyes, *J. Hazard. Mater.* 192 (2011) 786–793.
- [16] G.F. Yu, Y.X. Wang, H.B. Cao, H. Zhao, Y.B. Xie, Reactive oxygen species and catalytic active sites in heterogeneous catalytic ozonation for water purification, *Environ. Sci. Technol.* 54 (2020) 5931–5946.
- [17] Q. Zhu, J. Zhang, Is g-C₃N₄ more suitable for photocatalytic reduction or oxidation in environmental applications? *Environ. Funct. Mater.* 1 (2022) 121–125.
- [18] L. Shi, L.Q. Yang, W. Zhou, Y.Y. Liu, L.S. Yin, X. Hai, H. Song, J.H. Ye, Photoassisted construction of hole defective g-C₃N₄ photocatalysts for efficient visible-light-driven H_2O_2 production, *Small* 14 (2018), 1703142.
- [19] Y. Wu, H.N. Che, B. Liu, Y.H. Ao, Promising materials for photocatalysis-self-Fenton system: properties, modifications, and applications, *Small Struct.* 4 (2023), 2200371.
- [20] S.Q. Zhou, Y. Wang, K. Zhou, D.Y. Ba, Y.H. Ao, P.F. Wang, In-situ construction of Z-scheme g-C₃N₄/WO₃ composite with enhanced visible-light responsive performance for nitenpyram degradation, *Chin. Chem. Lett.* 32 (2021) 2179–2182.
- [21] J.J. Liu, H. Li, J. Zhang, Z.R. Shen, Boosting the photocatalytic activation of molecular oxygen and photodegradation of tetracycline: the role of interfacial synergistic effect of cocatalyst and dopants, *J. Colloid Interface Sci.* 628 (2022) 637–648.
- [22] H.N. Che, C.M. Li, C.X. Li, C.B. Liu, H.J. Dong, X.H. Song, Benzoyl isothiocyanate as a precursor to design of ultrathin and high-crystalline g-C₃N₄-based donor-acceptor conjugated copolymers for superior photocatalytic H_2 production, *Chem. Eng. J.* 410 (2021), 127791.
- [23] L. Zhou, J.R. Feng, B.C. Qiu, Y. Zhou, J.Y. Lei, M.Y. Xing, L.Z. Wang, Y.B. Zhou, Y. D. Liu, J.L. Zhang, Ultrathin g-C₃N₄ nanosheet with hierarchical pores and desirable energy band for highly efficient H_2O_2 production, *Appl. Catal. B: Environ.* 267 (2019), 118396.
- [24] S. Samanta, R. Yadav, A. Kumar, A.K. Sinha, R. Srivastava, Surface modified C, O co-doped polymeric g-C₃N₄ as an efficient photocatalyst for visible light assisted CO₂ reduction and H_2O_2 production, *Appl. Catal. B: Environ.* 259 (2019), 118054.
- [25] J. Ma, R. Long, D. Liu, J.X. Low, Y.J. Xiong, Defect engineering in photocatalytic methane conversion, *Small Struct.* 3 (2021), 2100147.
- [26] Y.H. Lv, Y.F. Liu, Y.Y. Zhu, Y.F. Zhu, Surface oxygen vacancy induced photocatalytic performance enhancement of a BiPO₄ nanorod, *J. Mater. Chem. A* 2 (2014) 1174–1182.
- [27] D.M. Chen, Z.H. Wang, T.Z. Ren, H. Ding, W.Q. Yao, R.L. Zong, Y.F. Zhu, Influence of defects on the photocatalytic activity of ZnO, *J. Phys. Chem. C.* 118 (2014) 15300–15307.
- [28] G.H. Dong, W.K. Ho, C.Y. Wang, Selective photocatalytic N₂ fixation dependent on g-C₃N₄ induced by nitrogen vacancies, *J. Mater. Chem. A* 3 (2015) 23435–23441.
- [29] X.Q. Fan, L.X. Zhang, M. Wang, W.M. Huang, Y.K. Zhou, M.L. Li, R.L. Cheng, J. L. Shi, Constructing carbon-nitride-based copolymers via Schiff base chemistry for visible-light photocatalytic hydrogen evolution, *Appl. Catal. B: Environ.* 182 (2016) 68–73.
- [30] Y. Yu, Y. Wei, W.Y. Gao, P. Li, X.F. Wang, S.M. Wu, W.G. Song, K.J. Ding, Aromatic ring substituted g-C₃N₄ for enhanced photocatalytic hydrogen evolution, *J. Mater. Chem. A* 5 (2017) 17199–17203.
- [31] Y. Wu, J. Chen, H.N. Che, X. Gao, Y.H. Ao, P.F. Wang, Boosting 2e⁻ oxygen reduction reaction in garland carbon nitride with carbon defects for high-efficient photocatalysis-self-Fenton degradation of 2,4-dichlorophenol, *Appl. Catal. B: Environ.* 307 (2022), 121185.
- [32] X. Zhang, P.J. Ma, C. Wang, L.Y. Gan, X.J. Chen, P. Zhang, Y. Wang, H. Li, L. H. Wang, X.Y. Zhou, K. Zheng, Unraveling the dual defect sites in graphite carbon nitride for ultra-high photocatalytic H_2O_2 evolution, *Energy Environ. Sci.* 15 (2022) 830–842.
- [33] Y.L. Zhu, Y.Y. Sun, J. Khan, H. Liu, G.L. He, X.T. Liu, J.M. Xiao, H.J. Xie, L. Han, NaClO-induced sodium-doped cyano-rich graphitic carbon nitride nanosheets with nitrogen vacancies to boost photocatalytic hydrogen peroxide production, *Chem. Eng. J.* 443 (2022), 136501.
- [34] S.B. Yang, Y.J. Gong, J.S. Zhang, L. Zhan, L.L. Ma, Z.Y. Fang, R. Vajtai, X.C. Wang, P.M. Ajayan, Exfoliated graphitic carbon nitride nanosheets as efficient catalysts for hydrogen evolution under visible light, *Adv. Mater.* 25 (2013) 2452–2456.
- [35] L. Chen, C. Chen, Z. Yang, S. Li, C.H. Chu, B.L. Chen, Simultaneously tuning band structure and oxygen reduction pathway toward high-efficient photocatalytic hydrogen peroxide production using cyano-rich graphitic carbon nitride, *Adv. Funct. Mater.* 31 (2021), 2105731.
- [36] H.-i Kim, Y. Choi, S. Hu, W. Choi, J.-H. Kim, Photocatalytic hydrogen peroxide production by anthraquinone-augmented polymeric carbon nitride, *Appl. Catal. B: Environ.* 229 (2018) 121–129.
- [37] C.H. Chu, Q.H. Zhu, Z.H. Pan, S. Gupta, D.H. Huang, Y.H. Du, S. Weon, Y.S. Wu, C. Muñich, E. Stavitski, K. Domen, J.-H. Kim, Spatially separating redox centers on 2D carbon nitride with cobalt single atom for photocatalytic H_2O_2 production, *Proc. Natl. Acad. Sci. U. S. A.* 117 (2020) 6376–6382.
- [38] Y.P. Yuan, L.S. Yin, S.W. Cao, L.N. Gu, G.S. Xu, P.W. Du, H. Choi, Y.S. Liao, C. Xue, Microwave-assisted heating synthesis: a general and rapid strategy for large-scale production of highly crystalline g-C₃N₄ with enhanced photocatalytic H_2 production, *Green. Chem.* 16 (2014) 4663–4668.
- [39] J. Tian, D. Wang, S. Li, Y. Pei, M.H. Qiao, Z.H. Li, J.L. Zhang, B.N. Zong, KOH-assisted band engineering of polymeric carbon nitride for visible light photocatalytic oxygen reduction to hydrogen peroxide, *ACS Sustain. Chem. Eng.* 8 (2019) 594–603.
- [40] Y.Y. Huang, D. Li, Z.Y. Fang, R.J. Chen, B.F. Luo, W.D. Shi, Controlling carbon self-doping site of g-C₃N₄ for highly enhanced visible-light-driven hydrogen evolution, *Appl. Catal. B: Environ.* 254 (2019) 128–134.
- [41] K.F. Wang, D.K. Shao, L. Zhang, Y.Y. Zhou, H.P. Wang, W.Z. Wang, Efficient piezocatalytic hydrogen peroxide production from water and oxygen over graphitic carbon nitride, *J. Mater. Chem. A* 7 (2019) 20383–20389.
- [42] H.J. Yu, R. Shi, Y.X. Zhao, T. Bian, Y.F. Zhao, C. Zhou, G.I.N. Waterhouse, L.Z. Wu, C.H. Tung, T.R. Zhang, Alkali-assisted synthesis of nitrogen deficient graphitic carbon nitride with tunable band structures for efficient visible-light-driven hydrogen evolution, *Adv. Mater.* 29 (2017), 1605148.
- [43] C. Hu, F. Chen, Y.G. Wang, N. Tian, T.Y. Ma, Y.H. Zhang, H.W. Huang, Exceptional cocatalyst-free photo-enhanced piezocatalytic hydrogen evolution of carbon nitride nanosheets from strong in-plane polarization, *Adv. Mater.* 33 (2021), 2101751.
- [44] X. Jiang, F. Yu, D. Wu, L. Tian, L. Zheng, L. Chen, P. Chen, L. Zhang, H. Zeng, Y. Chen, J. Zou, Sotypic heterojunction based on Fe-doped and terephthalaldehyde-modified carbon nitride for improving photocatalytic degradation with simultaneous hydrogen production, *Chin. Chem. Lett.* 32 (2021) 2782–2786.
- [45] S.W. Han, S.W. Joo, T.H. Ha, Y. Kim, K. Kim, Adsorption characteristics of anthraquinone-2-carboxylic acid on gold, *J. Phys. Chem. B* 104 (2000) 11987–11995.
- [46] Z.Y. Fang, Y.J. Bai, L.H. Li, D. Li, Y.Y. Huang, R.J. Chen, W.Q. Fan, W.D. Shi, In situ constructing intramolecular ternary homojunction of carbon nitride for efficient photoinduced molecular oxygen activation and hydrogen evolution, *Nano Energy* 75 (2020), 104865.
- [47] J. Colina-Marquez, F. Machuca-Matinez, G. Li Puma, Radiation absorption and optimization of solar photocatalytic reactors for environmental applications, *Environ. Sci. Technol.* 44 (2010) 5112–5120.
- [48] D. Dolat, N. Quici, E. Kusiak-Nejman, A.W. Morawski, G. Li Puma, One-step, hydrothermal synthesis of nitrogen, carbon co-doped titanium dioxide (N, C-TiO₂) photocatalysts. Effect of alcohol degree and chain length as carbon dopant precursors on photocatalytic activity and catalyst deactivation, *Appl. Catal. B: Environ.* 115–116 (2012) 81–89.
- [49] J. Xiong, X.B. Li, J.T. Huang, X.M. Gao, Z. Chen, J.Y. Liu, H. Li, B.B. Kang, W. Q. Yao, Y.F. Zhu, CN/rGO@BPQDs high-low junctions with stretching spatial charge separation ability for photocatalytic degradation and H_2O_2 production, *Appl. Catal. B: Environ.* 266 (2020), 118602.
- [50] G. Li Puma, A. Brucato, Dimensionless analysis of slurry photocatalytic reactors using two-flux and six-flux radiation absorption-scattering models, *Catal. Today* 122 (2007) 78–90.
- [51] G. Li Puma, Dimensionless analysis of photocatalytic reactors using suspended solid photocatalysts, *Chem. Eng. Res. Des.* 83 (2005) 820–826.
- [52] Y. Yang, C. Zhang, D.L. Huang, G.M. Zeng, J.H. Huang, C. Lai, C.Y. Zhou, W. J. Wang, H. Guo, W.J. Xue, R. Deng, M. Cheng, W.P. Xiong, Boron nitride quantum dots decorated ultrathin porous g-C₃N₄: intensified exciton dissociation and charge transfer for promoting visible-light-driven molecular oxygen activation, *Appl. Catal. B: Environ.* 245 (2019) 87–99.
- [53] T. Lu, Q.X. Chen, Independent gradient model based on Hirshfeld partition: a new method for visual study of interactions in chemical systems, *J. Comput. Chem.* 43 (2022) 539–555.
- [54] L.F. Cui, P.F. Wang, H.N. Che, X. Gao, J. Chen, B. Liu, Y.H. Ao, Co nanoparticles modified N-doped carbon nanosheets array as a novel bifunctional photothermal membrane for simultaneous solar-driven interfacial water evaporation and

- persulfate mediating water purification, *Appl. Catal. B: Environ.* 330 (2023), 122556.
- [55] J.N. Li, J. Chen, Y.H. Ao, X. Gao, H.N. Che, P.F. Wang, Prominent dual Z-scheme mechanism on phase junction WO_3/CdS for enhanced visible-light-responsive photocatalytic performance on imidacloprid degradation, *Sep. Purif. Technol.* 281 (2022), 119863.
- [56] X. Gao, J. Chen, H.N. Che, Y.H. Ao, P.F. Wang, Rationally constructing of a novel composite photocatalyst with multi charge transfer channels for highly efficient sulfamethoxazole elimination: mechanism, degradation pathway and DFT calculation, *Chem. Eng. J.* 426 (2021), 131585.
- [57] J.Y. Hu, X.P. Jing, L. Zhai, J. Guo, K. Lu, L. Mao, BiOCl facilitated photocatalytic degradation of atenolol from water: reaction kinetics, pathways and products, *Chemosphere* 220 (2019) 77–85.
- [58] D. Miao, J.B. Peng, X.H. Zhou, L. Qian, M.J. Wang, L. Zhai, S.X. Gao, Oxidative degradation of atenolol by heat-activated persulfate: kinetics, degradation pathways and distribution of transformation intermediates, *Chemosphere* 207 (2018) 174–182.
- [59] Z.M. He, H.P. Yang, N.H. Wong, L. Ernawati, J. Sunarso, Z.Y. Huang, Y.M. Xia, Y. Wang, J.B. Su, X.F. Fu, M. Wu, Construction of $\text{Cu}_7\text{S}_4@\text{CuCo}_2\text{O}_4$ yolk-shell microspheres composite and elucidation of its enhanced photocatalytic activity, mechanism, and pathway for carbamazepine degradation, *Small* 19 (2023), 2207370.
- [60] C.M. Li, Y.H. Du, D.P. Wang, S.M. Yin, W.G. Tu, Z. Chen, M. Kraft, G. Chen, R. Xu, Unique P-Co-N surface bonding states constructed on g-C₃N₄ nanosheets for drastically enhanced photocatalytic activity of H₂ evolution, *Adv. Funct. Mater.* 27 (2017), 1604328.
- [61] H.N. Che, J. Wang, P.F. Wang, Y.H. Ao, J. Chen, X. Gao, F.Y. Zhu, B. Liu, Simultaneously achieving fast intramolecular charge transfer and mass transport in holey D-π-A organic conjugated polymers for highly efficient photocatalytic pollutant degradation, *JACS Au* 3 (2023) 1424–1434.
- [62] H.N. Che, P.F. Wang, J. Chen, X. Gao, B. Liu, Y.H. Ao, Rational design of donor-acceptor conjugated polymers with high performance on peroxydisulfate activation for pollutants degradation, *Appl. Catal. B: Environ.* 316 (2022), 121611.
- [63] Y. Zhang, J. Di, P.H. Ding, J.Z. Zhao, K.Z. Gu, X.L. Chen, C. Yan, S. Yin, J.X. Xia, H. M. Li, Ultrathin g-C₃N₄ with enriched surface carbon vacancies enables highly efficient photocatalytic nitrogen fixation, *J. Colloid Interface Sci.* 553 (2019) 530–539.
- [64] J.S. Zhang, M.W. Zhang, R.Q. Sun, X.C. Wang, A facile band alignment of polymeric carbon nitride semiconductors to construct isotype heterojunctions, *Angew. Chem. Int. Ed.* 51 (2012) 10145–10149.
- [65] Y. Xiao, Y.L. Tao, Y.H. Jiang, J. Wang, W.L. Zhang, Y. Liu, J.M. Zhang, X.Y. Wu, Z. C. Liu, Construction of core-shell CeO₂ nanorods/SnIn₄S₈ nanosheets heterojunction with rapid spatial electronic migration for effective wastewater purification and H₂O₂ production, *Sep. Purif. Technol.* 304 (2023), 122385.
- [66] R.R. Jiang, G.H. Lu, T.J. Dang, M. Wang, J.C. Liu, Z.H. Yan, H.J. Xie, Insight into the degradation process of functional groups modified polystyrene microplastics with dissolvable BiOBr-OH semiconductor-organic framework, *Chem. Eng. J.* 470 (2023), 144401.
- [67] H.N. Che, X. Gao, J. Chen, J. Hou, Y.H. Ao, P.F. Wang, Iodide-induced fragmentation of polymerized hydrophilic carbon nitride for high-performance quasi-homogeneous photocatalytic H₂O₂ production, *Angew. Chem. Int. Ed.* 60 (2021) 25546–25550.
- [68] W. Liu, P.F. Wang, J. Chen, X. Gao, H.N. Che, B. Liu, Y.H. Ao, Unraveling the mechanism on ultrahigh efficiency photocatalytic H₂O₂ generation for dual-heteroatom incorporated polymeric carbon nitride, *Adv. Funct. Mater.* 32 (2022), 2205119.